ADVANCED MATERIALS
www.advmat.de

Low Thermal Conductivity and Diffusivity at High Temperatures Using Stable High-Entropy Spinel Oxide Nanoparticles

*Ka Man Chung, Sarath R. Adapa, Yu Pei, Ram Hemanth Yeerella, Li Chen, Sashank Shivakumar, Wei Huang, Zhaowei Liu, Shengqiang Cai, Jian Luo, and Renkun Chen**

The realization of low thermal conductivity at high temperatures (0.11 W m^{-1} K^{-1} 800 °C) in ambient air in a porous solid thermal insulation material, using stable packed nanoparticles of high-entropy spinel oxide with 8 cations (HESO-8 NPs) with a relatively high packing density of ≈50%, is reported. The high-density HESO-8 NP pellets possess around 1000-fold lower thermal diffusivity than that of air, resulting in much slower heat propagation when subjected to a transient heat flux. The low thermal conductivity and diffusivity are realized by suppressing all three modes of heat transfer, namely solid conduction, gas conduction, and thermal radiation, via stable nanoconstriction and infrared-absorbing nature of the HESO-8 NPs, which are enabled by remarkable microstructural stability against coarsening at high temperatures due to the high entropy. This work can elucidate the design of the next-generation high-temperature thermal insulation materials using high-entropy ceramic nanostructures.

1. Introduction

Thermal insulation at high temperatures is essential for performance, durability, and safety in various applications.[1] For example, thermal barrier coatings, mainly consisting of low-thermal conductivity metal oxides, are used as excellent thermal insulation layers to enable the operation of gas turbine engines for aerospace and electricity generation applications at high temperatures (i.e., >1300 °C).[2] Solid oxide fuel cells (SOFCs) operating at high operating temperatures of 800–1000 °C require thermal insulation layers with high thermal and chemical stability.[3] Thermal runaway in lithium-ion batteries, which could lead to temperatures as high as 1000 °C,[4] could be mitigated by delaying heat propagation with a thin thermal barrier.[5] Other important high-temperature applications include firefighting protective clothing,[6] hypersonic vehicles,[7] space re-entry vehicles,[8] and spacecraft (e.g., Parker Solar Probe[9]).

A desirable thermal insulation material should exhibit low thermal conductivity (k), which measures how much heat can conduct through the material when subjected to a steady heat source. However, an important but often overlooked property is thermal diffusivity ($\alpha = \frac{k}{\rho C_p}$, where ρ is the density and C_p is the specific heat capacity), which characterizes how fast the heat can propagate through the material under a *transient* heat flux. Additionally, the mechanical strength of the material is also important when there is a structural loading applied to the material. Unfortunately, there is usually a tradeoff between the thermal insulation properties and mechanical strength (**Figure 1a**). On one hand, dense thermal insulation materials, such as metal oxides (e.g., yttria-stabilized zirconia or YSZ), have good strength but relatively high thermal conductivity, around 2.0 W m^{-1} K^{-1} at 1000 °C.[10] While various phonon scattering strategies have been engineered to reduce the thermal conductivity,[11] there exists a lower limit to the phonon scattering approach which occurs when the phonon mean free path is comparable to interatomic distances in solids, known as the amorphous limit[12] or diffuson thermal conductivity.[13] For dense solids, this limit is about 1 W m^{-1} K^{-1}.[12,13]

On the other hand, porous nanostructures, such as aerogels,[14–17] graphene scaffolds,[18,19] fibers,[20] porous refractory bricks,[21] and foams,[22,23], usually possess lower thermal conductivity, but at the expense of poor mechanical

K. M. Chung, L. Chen, S. Shivakumar, W. Huang, Z. Liu, S. Cai, J. Luo, R. Chen
Program in Materials Science and Engineering
University of California
San Diego, La Jolla, CA 92093, USA
E-mail: rkchen@ucsd.edu
S. R. Adapa, Y. Pei, R. H. Yeerella, S. Cai, R. Chen
Department of Mechanical and Aerospace Engineering
University of California
San Diego, La Jolla, CA 92093, USA
L. Chen, Z. Liu
Department of Electrical and Computer Engineering
University of California San Diego
La Jolla, CA 92093, USA
S. Shivakumar, W. Huang, J. Luo
Aiiso Yu Feng Li Family Department of Chemical and Nano Engineering
University of California San Diego
La Jolla, CA 92093, USA
The ORCID identification number(s) for the author(s) of this article can be found under https://doi.org/10.1002/adma.202406732

DOI: 10.1002/adma.202406732

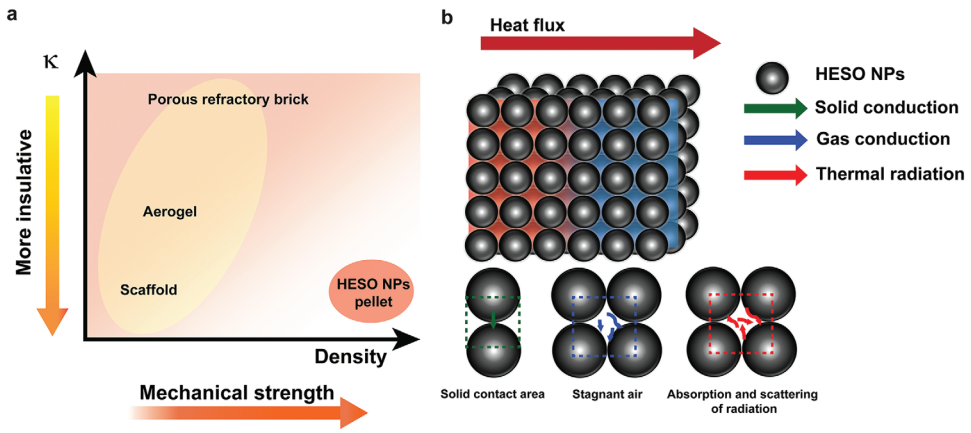

Figure 1. Strategy of achieving ultralow thermal conductivity and diffusivity using stable HESO-8 NP pellets at high temperature. a) Schematic showing the typical positive correlation between thermal conductivity (κ) and mechanical strength, represented by the density of high-temperature porous thermal insulation materials. Our HESO-8 NP pellets possess a desirable and unique combination of better thermal insulation (low thermal conductivity and diffusivity) and higher mechanical strength. b) Schematic of HESO-8 NP pellet and the heat transfer mechanisms. All heat transfer pathways, including solid conduction, gas conduction, and thermal radiation, are suppressed, as illustrated by the reduced pathways.

strength. Additionally, there are often competing effects of the porosity on different heat transfer pathways in a porous material. The effective thermal conductivity of porous structures can be expressed in the general form[11]

$$\kappa = \kappa_{solid} + \kappa_{gas} + \kappa_{rad} \quad (1)$$

where κ_{solid}, κ_{gas}, and κ_{rad} are the heat conduction through the solid phase, interstitial gas, and thermal radiation, respectively. A higher porosity can reduce κ_{solid} by limiting the solid matrix contact areas and enhancing phonon boundary scattering. However, heat conduction through gas becomes dominant and the porous material thus attains a gas-like thermal conductivity, for instance, air thermal conductivity (e.g., k_{air} = 0.026–0.080 W m^{-1} K^{-1} from 25 to 1000 °C). κ_{gas} can be further reduced when the pore size is comparable to the mean free path of the stagnant gas, namely the Knudsen effect.[24] However, high porosity and nanoscale pore size lead to high transmittance of infrared (IR) photons in the material and consequently high κ_{rad} at high temperature, which scales with temperature (T) as T^3. For example, κ of silica aerogel is 0.02 W m^{-1} K^{-1} in ambient air at room temperature but increases to 0.20 W m^{-1} K^{-1} at 600 °C mainly due to the increase in κ_{rad}.[25]

In 2006, Prasher[26] predicted low thermal conductivity using packed NPs. The theoretical results show that by choosing NPs with suitable physical properties, including particle sizes, bulk thermal conductivity, surface energy, etc., the packed NPs can achieve a thermal conductivity lower than that of air. This concept was partially experimentally realized at room temperature,[27] with packed alumina NPs having a thermal conductivity of 0.035 W m^{-1} K^{-1}, or about 40% higher than that of air. However, the IR transparency of alumina[28] would have led to high radiation thermal conductivity at high temperatures.

Herein, we report low thermal conductivity at high temperatures in ambient air using packed NP pellets of high-entropy spinel oxide with 8 cations (HESO-8 NPs) with a composition of (Co, Mg, Mn, Ni, Zn)(Al, Co, Cr, Fe, Mn)$_2$O$_4$. Different from conventional thermal insulation materials with porous structures, the HESO-8 NP pellets reported in our work exhibit both a high relative density of ≈50% with high mechanical strength and low thermal conductivity and diffusivity (Figure 1a). Figure 1b shows the mechanisms of suppressing all three heat transfer pathways, including solid conduction due to small contact areas between NPs, gas conduction originated from confined interstitial spaces between NPs, and thermal radiation contributed by IR-absorbing metallic spinel oxides. The thermal conductivity of HESO-8 NP pellets from room temperature to 800 °C was measured and showed a nearly constant trend up to 800 °C (0.11 W m^{-1} K^{-1} at 800 °C), where it was much lower than aerogels (0.2 W m^{-1} K^{-1} at 600 °C).[25] More importantly, due to its relatively high packing density, the thermal diffusivity of HESO-8 NP pellets is over 1000-fold lower than that of air (0.046 mm^2 s^{-1} vs 55 mm^2 s^{-1} at 800 °C). HESO-8 NPs in our work show excellent sintering (coarsening) resistance. The thermal conductivity and particle size remain nearly unchanged after high-temperature thermal treatment up to 800 °C. The work sheds new light on the design of the next-generation thermal insulation materials.

2. Results and Discussion

2.1. Materials Characterization

HESO-8 NPs with a composition of (Co, Mg, Mn, Ni, Zn)(Al, Co, Cr, Fe, Mn)$_2$O$_4$ were synthesized,[29] along with control samples of high-entropy spinel oxide with 6 and 5 cations (HESO-6 and HESO-5), namely $(Co_{1/6}Cr_{1/6}Cu_{1/6}Fe_{1/6}Mn_{1/6}Ni_{1/6})_3O_4$ and $(Co_{1/5}Cr_{1/5}Fe_{1/5}Mn_{1/5}Ni_{1/5})_3O_4$,[30] and a simple spinel oxide, $CuCr_2O_4$.[31] The microstructural stability against coarsening at high temperatures of the HESO-8 NPs is shown upon heat treatment compared to the other spinel oxide NPs. As shown in **Figure 2a,d**, as-synthesized HESO-5, HESO-6, and HESO-8 NPs originally exhibited nano-scale particle sizes. After heat treatment at 1000 °C for 100 h, HESO-5, and HESO-6 NPs grew into a few micrometers in average size. The HESO-8 NPs, on

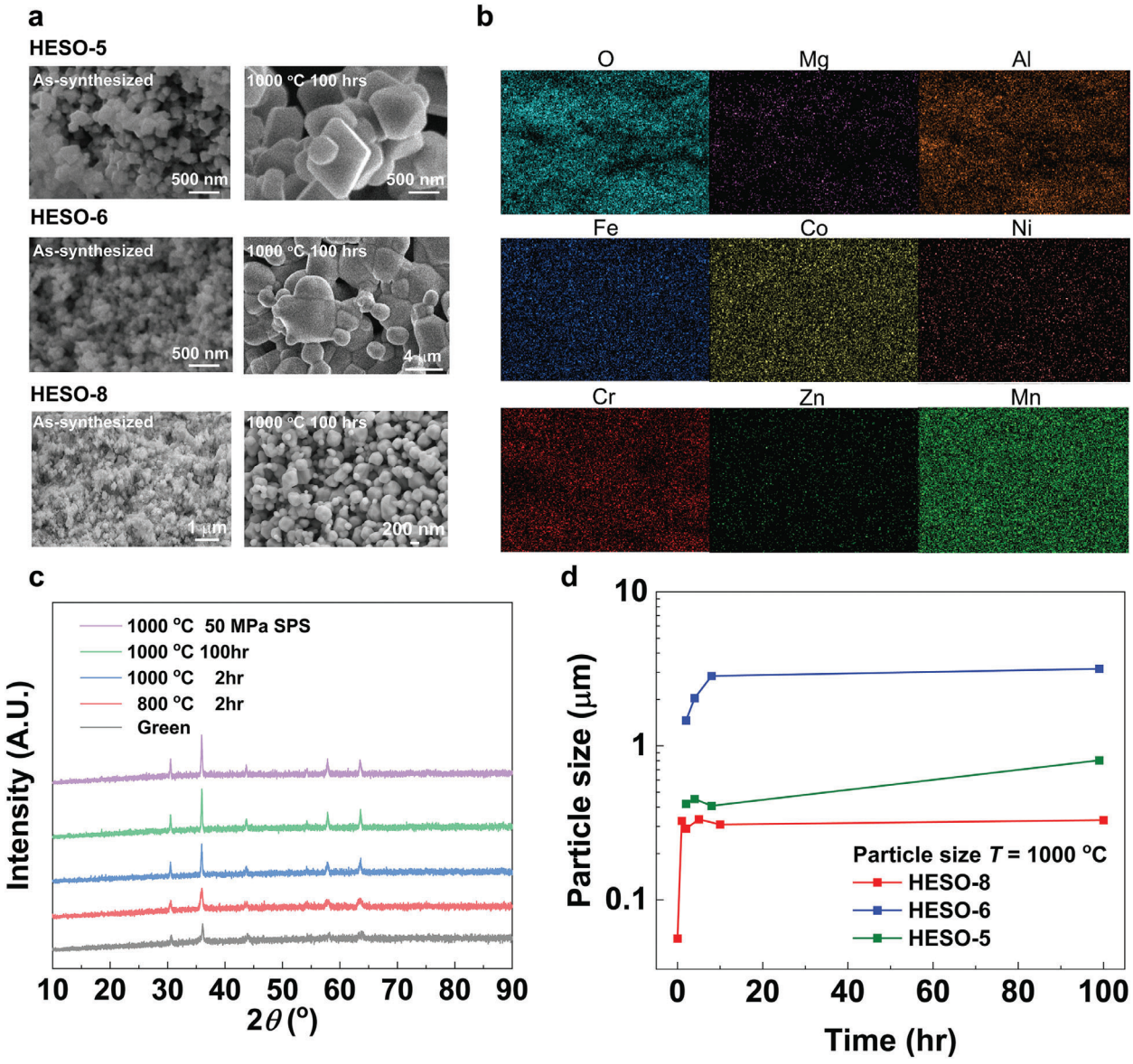

Figure 2. Characterization of spinel oxide NPs. a) SEM images of spinel oxide NPs, including HESO-5, HESO-6, and HESO-8 NPs respectively, before and after a heat treatment at 1000 °C for 100 hrs; b) EDS mapping of HESO-8 NPs showing its compositional homogeneity upon thermal treatment at high temperatures (1000 °C). c) XRD patterns of HESO-8 NPs upon different heat treatments. d) Particle size evolution of spinel oxide NPs upon different time intervals of the heat treatments. The particle sizes were estimated based on the SEM images of the NPs after the heat treatments.

the other hand, show excellent particle size stabilization. The particle growth was limited to <500 nm even after a heat treatment at 1000 °C for 100 h. The chemical homogeneity of HESO-8 NPs was confirmed using EDS mapping which shows that the 8 cations are uniformly distributed across the sample (Figure 2b). HESO-8 NPs also have high phase stability, as revealed in the XRD patterns. It exhibits a single spinel structure upon synthesis and high-temperature heat treatment at 800 and 1000 °C, and spark plasma sintering (SPS) (Figure 2c).

Figure 3a shows the thermogravimetric analysis (TGA) results of HESO-8 NP pellets before and after 1000 °C thermal annealing. As prepared HESO-8 sample has an overall weight change of around 2% which might include moisture and other impurity removal. For thermally annealed HESO-8, the weight change is negligible. It further confirms the high-temperature stability of the HESO-8 NP pellets. The optical absorptance of the HESO-8 NP pellets before and after 1000 °C thermal annealing for 2 hr is shown in Figure 3b. The results show that HESO-8 NPs are highly absorptive for the entire spectrum, due to the metallic nature of the spinel oxides and the nanoscale porosity that gives rise to the light trapping effect. The absorptance did not change after the thermal treatment, also revealing the stability of the nanoscale porosity of the HESO-8 NP pellets. This high IR absorptance will lead to negligible radiation thermal conductivity [κ_{rad} in Equation (1)]. The average elastic modulus (E) and hardness (h) of each pellet are shown in Figure 3c. The mechanical

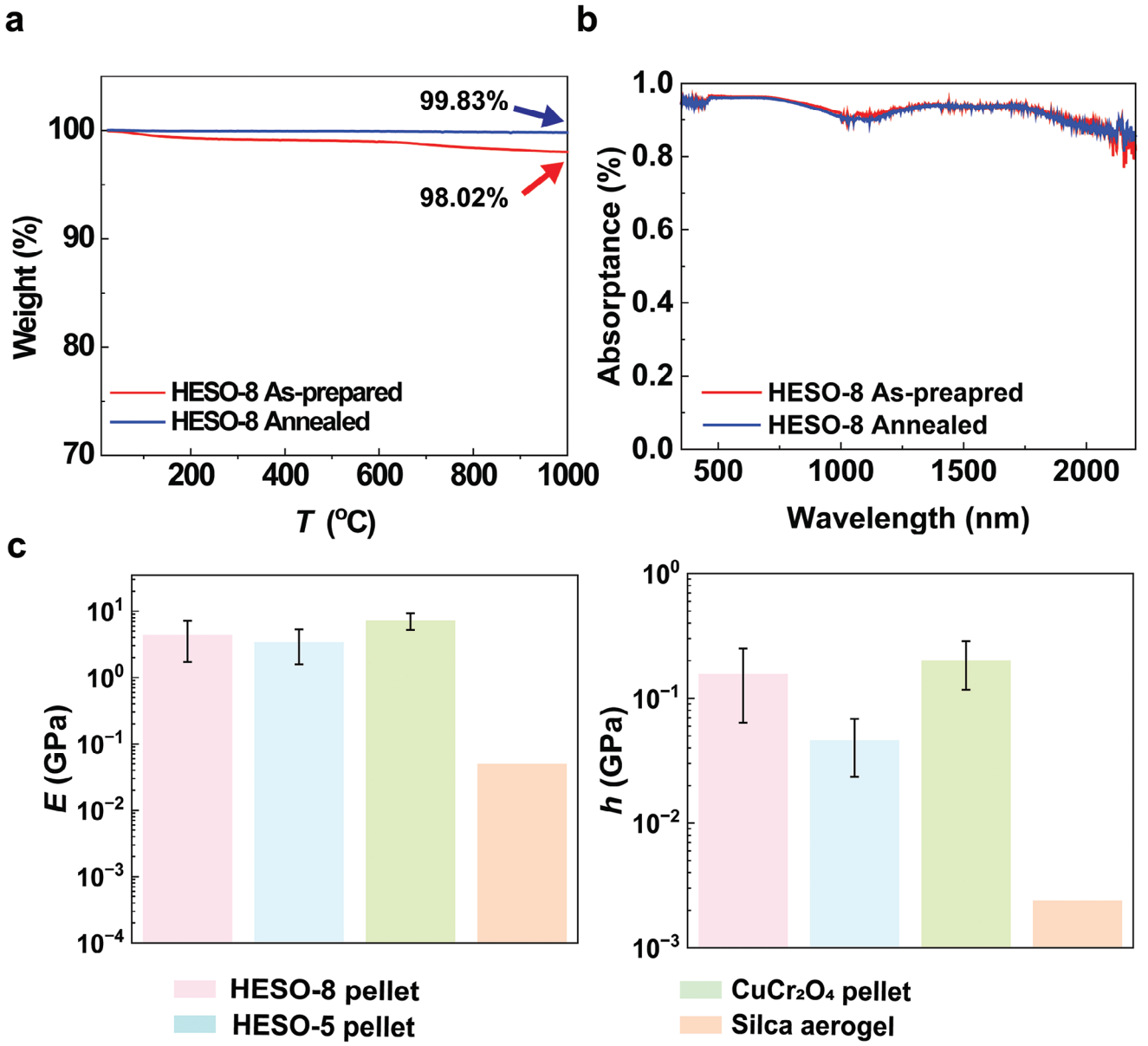

Figure 3. Characterization of HESO NP pellets. a) TGA results of HESO-8 NPs up to 1000 °C showing their high thermal stability. b) Optical absorbance of HESO-8 NP pellets in the wavelength from 350 to 2200 nm at room temperature. c) Mechanical property measurement results of HESO-8 NP pellets, other packed spinel oxides, including HESO-5, $CuCr_2O_4$, and literature data on a silica aerogel with around 5% relative density.[32]

data has relatively large errors due to the rough surfaces of the pellets. Nevertheless, the data show that all the HESO NP pellets have two orders of magnitude higher E and h than those of silica aerogels with around 5% relative density,[32] meaning that they can withstand much higher mechanical loads. The raw data of the mechanical test is included in Figure S9 (Supporting Information).

2.2. Thermal Conductivity and Thermal Diffusivity

Thermal conductivity of the pellets was measured using laser flash analysis (LFA) which directly measures thermal diffusivity (α) (**Figure 4a**). The thermal conductivity is obtained using the following relation: $k = \rho C_p \alpha$ where C_p is specific heat, ρ is the measured density of the pellets. Figure 4b shows the κ versus T plot of the HESO-8 pellets, made from HESO-8 NPs annealed at 1000 °C in air. The reported values of the state-of-the-art thermal insulation materials were plotted alongside for comparison.[15,17,19,21] A more comprehensive measured thermal conductivity comparison of the HESO NP pellets to various thermal insulation materials reported in refs. [15–17,19,21,22,33] is included in Table S1 (Supporting Information). When T increases from room temperature to 800 °C, κ of HESO-8 NP pellets show a small increase from 0.06 to 0.11 W m^{-1} K^{-1}. The HESO-8 pellets possess a lower thermal conductivity at

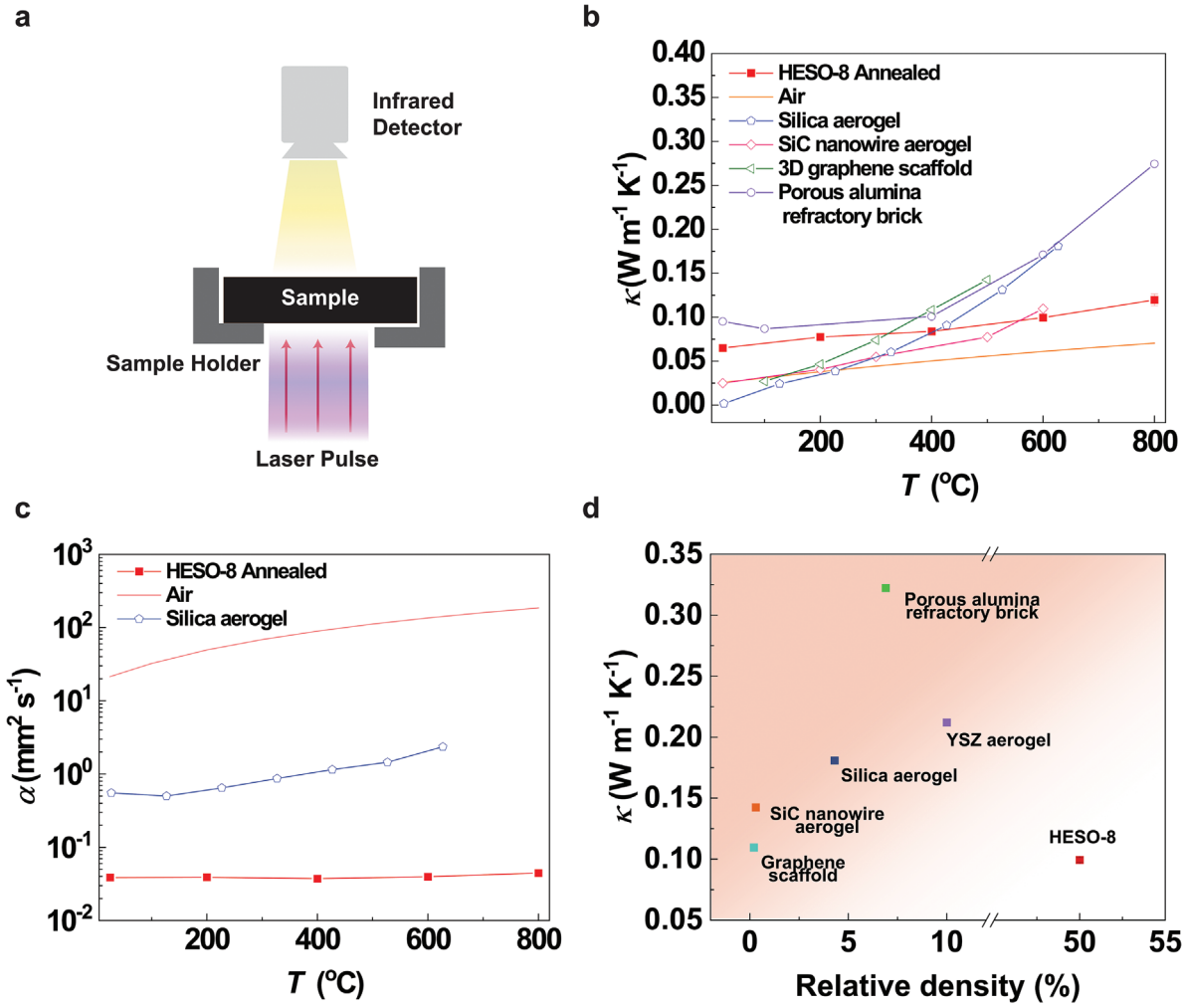

Figure 4. Thermal conductivity and diffusivity of the HESO NP pellets. a) Schematic of the LFA thermal diffusivity measurement setup. b) Measured κ versus T of HESO-8 NP pellets up to 800 °C. The reported literature results of the other thermal insulation materials from refs. [15,17,19,21] are plotted alongside for comparison. c) α versus T of packed HESO-8 NP pellet, HESO-5 NP pellet, and $CuCr_2O_4$ NP pellet up to 800 °C. α of air and a 5% silica aerogel are plotted alongside for comparison. The thermal transport property data of 5% silica aerogel is from ref. [17]. d) Summary of κ versus relative density of HESO-8 NP and reported samples at their highest measured temperature, including SiC nanowire aerogel,[15] graphene scaffolds,[19] 5% silica aerogel,[17] YSZ-aerogel,[16] and porous alumina refractory brick.[21]

high temperatures among all the materials reported to date, such as aerogels. The HESO-8 NP pellet with thermal annealing at 1000 °C shows the same and repeatable thermal conductivity trend for the entire temperature range, revealing the excellent thermal stability of the HESO-8 NP pellet. It is consistent with the materials characterization results as shown in Figures 2 and 3.

Figure 4c summarizes the measured α of pellets made of HESO-8 NPs with the reported values of air and the 5% silica aerogel for comparison. The HESO-8 NP pellets show a near-constant α in the entire temperature range from room temperature to 800 °C. It is about 1000 times lower than that of air (0.04 vs 135 $mm^2\ s^{-1}$ at 600 °C) and about two orders of magnitude lower than that of the 5% silica aerogel at 600 °C. This is because the HESO-8 NP pellets have low thermal conductivity and much higher packing density than typical thermal insulation materials.

2.3. Transient Thermal Insulation Test

The transient thermal insulation capability of the HESO-8 NP pellets was tested using a home-built setup (**Figure 5**a) and compared to traditional thermal insulation materials, namely, air, fiberglass, and porous refractory fire brick. Upon heating by a propane blowtorch, a stainless-steel shim inserted on the front side of the samples experienced a temperature rise to ≈850 °C in 30 s. After the shim sheet reached thermal equilibrium, the heat was then transferred to the samples. Figure 5b shows the backside temperature rise of the samples as a function of time. It shows that air, fiberglass, and refractory fire brick quickly reached their maximum temperature and plateaued in less than 120 s. It is consistent with higher thermal diffusivity of air, fiberglass, and fire brick. On the other hand, the HESO-8 NP pellet displayed a much slower temperature rise. It took about 20 min (or 10× longer time) for the HESO-8 NP pellet to reach the back

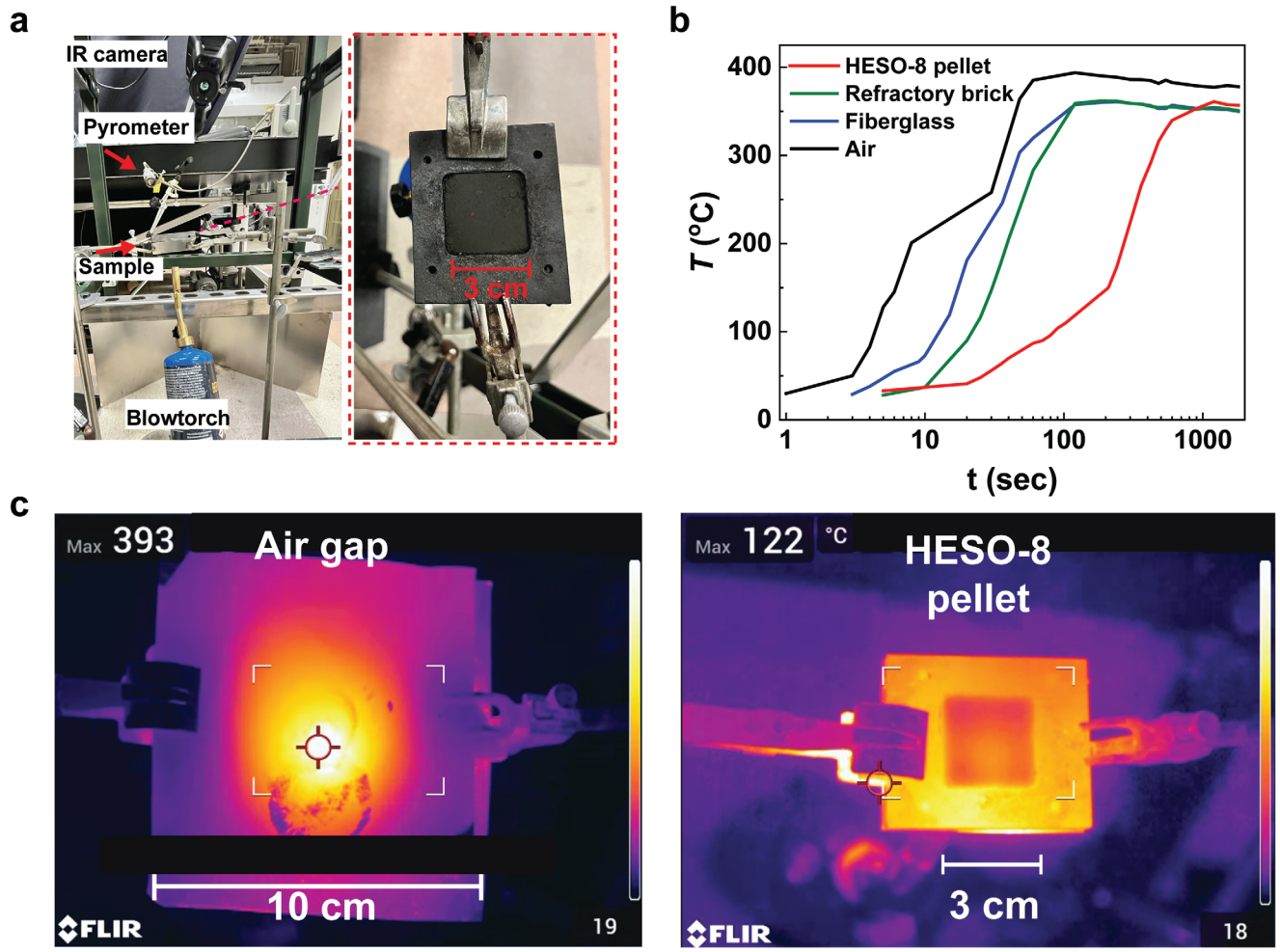

Figure 5. Transient thermal insulation test. a) Digital photo of the thermal insulation demonstration setup with the key components labeled. The enlarged photo shows the photo of the HESO-8 NP pellet (3 cm × 3 cm × 1 cm). b) Measured backside temperature as a function of time for different thermal insulation materials: air, fiberglass, porous refractory fire brick, and HESO-8 NP pellet. c) IR images of the backside of air (covered by a steel shim sheet) and HESO-8 NP pellets in the thermal insulation demonstration at 1 min upon blowtorch heating. Additional IR images of the fiberglass and the refractory fire brick can be found in Figure S10 (Supporting Information).

temperature equilibrium, which is attributed to the much lower thermal diffusivity (Figure 3d). The slower heat propagation in the HESO-8 NP pellet means lower temperature during the beginning phase of the heating. The IR images of the backside of air (covered by a steel shim sheet) and HESO-8 NP pellets after 1 min blowtorch heating are shown in Figure 5c. At 1 min after the torch heating, the HESO-8 NP pellet sample was about 122 °C on the backside, whereas that of air was 393 °C. Additional IR images of the fiberglass and the refractory fire brick are included in Figure S10 (Supporting Information). Similar to the case of air, the backside temperature of the fiberglass and the refractory fire brick was up to 344 and 276 °C, respectively, after 1 min blowtorch heating.

2.4. Discussion

HESO-8 NP pellets have outstanding thermal insulation ability compared to state-of-the-art thermal insulation materials, for example, SiC nanowire aerogel,[15] graphene scaffolds,[19] porous alumina refractory brick,[21] and a 5% silica aerogel.[17] It has a much lower k at high temperatures compared to these materials. Among the materials shown in the figure, HESO-8 NP pellets are the only materials that show air-like thermal conductivity at high temperatures in ambient air. The realization of ultra-low thermal conductivity of HESO-8 NPs at high temperatures is due to three reasons: 1) limited heat conduction through nanoscale constrictions at small solid contacts between NPs.[26,34] 2) Nanoscale interstitial voids between NPs with dimensions comparable to that of the mean free path of air. These two mechanisms have also been studied previously.[26,27,34] However, the remarkable high-temperature stability of the HESO-8 NPs is the key to maintaining the low solid and gaseous thermal conductivity enabled by nanoconstriction. (3) Suppression of thermal radiation in IR-absorbing metallic spinel oxide NPs,[35] as revealed from the optical measurement (Figure 3b). Importantly, these three mechanisms break the correlation between thermal conductivity and relative density in traditional thermal insulation material

illustrated in Figure 1a. As shown in Figure 4c, HESO-8 NP pellets have the highest density (≈2200 kg m^{-3}, relative density of ≈50%) while possessing the low thermal conductivity at the highest reported temperatures. Therefore, the HESO-8 NP pellets represent a counterintuitive and novel class of thermal insulation materials that has a unique combination of low thermal conductivity and high mechanical strength (Figure 1a).

Thermal conductivity of as-prepared (i.e., unannealed) HESO-5, HESO-6, and HESO-8 NP pellets and annealed HESO-8 NP pellet was measured. The results are included in Figure S1 (Supporting Information). While as-prepared HESO-5, HESO-6, and HESO-8 NP pellets showing higher thermal conductivity (0.3–0.4 W m^{-1} K^{-1}) at room temperature and substantial increases as a function of temperature, annealed HESO-8 NP pellet shows low and nearly constant thermal conductivity room temperature up to 800 °C (0.11 W m^{-1} K^{-1}), as displayed in Figure 4b. The superior thermal insulation ability of the annealed HESO-8 NP pellet at high temperatures can be explained by its thermal and particle size stability once the as-prepared particles quickly grew into slighly larger (~300 nm) but stablized particles upon annealing at 1000 °C (Figure 2d).

In terms of particle size stability, HESO-6, HESO-5, and $CuCr_2O_4$ show significant particle growth after thermal annealing at high temperatures (Figure 2a and Figures S2 and S3, Supporting Information). The origin of the particle size instability of HESO-6 (containing Co, Cr, Cu, Fe, Mn, and Ni) and $CuCr_2O_4$ NP is due to the instability of copper oxideoxide. Copper oxide is known for its reduction reaction of CuO to Cu_2O, and eventually to Cu metal.[36] We confirmed this with STA (DSC+TGA) measurements on CuO under synthetic Air. The STA results are included in Figures S4 and S5 (Supporting Information). This is consistent with the phase diagram of CuO.[36] Cu_2O melts at 1160 °C and eventually reduces to liquid Cu metal at 1500 °C. Molten Cu eats through the crucible indicated by the large mass loss and shown in Figure S4b (Supporting Information). It was observed that at high temperatures, $CuCr_2O_4$, the Cu(II) cation readily reduced to Cu(I), forming $Cu_2Cr_2O_4$. Figure S5 shows the STA measurement of as-prepared $CuCr_2O_4$ nanoparticles under synthetic air and in a Pt crucible. While the oxide stability increases from CuO to $CuCr_2O_4$ and to HESO-6, there is strong evidence that Cu is a highly volatile cation and is the most probable cause behind the high grain growth in HESO-6. While HESO-6 is peculiar due to Cu, the comparison between HESO-5 and HESO-8 (neither contains Cu) shows that the higher entropy in HESO-8 does contribute to better grain growth and sintering resistance.

To compare the effect of bulk thermal conductivity, bulk HESO materials (HESO-5 and HESO-8) were prepared using SPS and measured using LFA to obtain their intrinsic bulk thermal conductivity. The densities obtained were 4680 kg m^{-3} (93% dense) and 3590 kg m^{-3} (71% dense) for HESO-5 and HESO-8, respectively. From both the densities and particle-boundaries seen from SEM images shown in Figure S3 (Supporting Information), it suggests that HESO-8 is more sintering-resistant, as expected. HESO-8 has 40% lower measured thermal conductivity than that of the HESO-5 sample (≈1.5 vs ≈2.5 W m^{-1} K^{-1}), as shown in Figure S6 (Supporting Information). After the correction with relative densities (ψ = 71% and 93% for HESO-8 and HESO-5, respectively) using the Maxwell-Eucken model,[37] the bulk thermal conductivity (k_{bulk}) of these two samples is similar: 2.55 versus 2.35 W m^{-1} K^{-1} for HESO-5 and HESO-8, respectively, at 1000 °C. This is understandable because both samples have a very high degree of disorder, leading to strong phonon defect scattering and amorphous-like thermal conductivity at high temperatures in these crystalline materials. Given the similar k_{bulk} of HESO-5 and HESO-8, we may conclude that the superior thermal insulation exhibited by annealed HESO-8 compared to other HESO and spinel oxide NPs in our study are contributed by the nanoconstriction, enabled by its stable particle sizes and sintering resistance at high temperatures.

Given that the pellets in our study have packing densities ranging from 46% to 60% and very different particle size distributions, it is of interest to differentiate the packing density effect. We have performed a theoretical study using ZBS (Zehner, Bauer, and Schlünder) model for modeling particle bed thermal conductivity.[38] The modeling result is included in Figure S8 (Supporting Information). It shows that the packing densities (ψ) do not have a strong effect as long as the fractional contact area between the particles is the same (assumed to be 6% here). The modeling study further confirms the conclusion that the low thermal conductivity of the annealed HESO-8 NP pellets is enabled by the nanoconstriction formed by the sintering-resistant nanoparticles, providing a finite, small contact areas for thermal transport.

The origin of the excellent sintering and coarsening resistance of HESO-8 NPs needs further investigation. Such sintering and coarsening resistance have also been observed in other high-entropy material systems.[39,40] There is still a lack of a unified theory to account for this phenomenon. On the one hand, one may suggest that it is associated with the so-called "sluggish diffusion" of high-entropy materials.[41] However, it was reported that the number of components in the high-entropy materials does not affect the kinetic diffusion.[42] The proposed sluggish diffusion may not be a convincing explanation. On the other hand, high-entropy grain boundaries (HEGBs) were proposed as the grain boundary counterpart to high-entropy materials.[43] It was shown that HEGBs can stabilize nanocrystalline alloys at high temperatures against grain growth from the reducing thermodynamic driving forces and increasing kinetic impediment.[40,43,44] Similar thermodynamic and kinetic stabilizations may contribute to the suppression of particle growth and sintering of HESO-8 NPs, thereby enabling their high-temperature microstructural stability (against sintering and coarsening) to retain the nanoporous structure and good thermal insulations.

3. Conclusion

In summary, we report low thermal conductivity (0.11 W m^{-1} K^{-1} at 800 °C) and diffusivity (0.046 mm^2 s^{-1} at 800 °C) realized by using packed high-entropy spinel oxide NPs (HESO-8 NPs) under an ambient environment. Utilizing the unique features of the nano-constriction formed by the HESO-8 NPs, all three heat transfer mechanisms in porous structures, namely solidconduction, gas conduction, and thermal radiation, are suppressed. An air-like thermal conductivity of HESO-8 NP pellets can therefore be achieved without evacuation. Moreover, owing to the high packing density of the HESO-8 NP pellet compared to traditional thermal insulation material with high porosities, it exhibits 1000 times lower thermal diffusivity compared to air.

At the material level, taking advantage of the unusual particle size stabilization of high-entropy materials, the HESO-8 NPs show better sintering resistance and thermal stability compared to other traditional thermal insulation materials. The work can benefit the design of the next-generation thermal barrier materials for applications in various technologies such as gas turbine engines, buildings, and energy storage devices, where thermal insulation is critically important for safety and materials protection.

4. Experimental Section

Materials Synthesis and Preparation: (Co, Mg, Mn, Ni, Zn)(Al, Co, Cr, Fe, Mn)$_2O_4$ HESO-8 NPs with eight different cations were prepared using hydrothermal synthesis.[31] The constitutional water-soluble metal salts were weighted and dissolved in deionized (DI) water with specific mole concentrations. The as-prepared solutions were then mixed and stirred for 1 hr to enable compositional uniformity. To form precipitates, 10 M NaOH was added to the resultant solutions until a pH level of 11.5 was reached. The viscous solution was further mixed. It was then put in Teflon-lined autoclaves for thermal treatment at 200 °C for 24 hrs in an oven. After that, the solid sample obtained was washed with DI water and further purified using a centrifuge. The as-obtained solid sample was dried overnight in an oven of around 70 °C. They were then heated in a box furnace at 550 °C for 5 hrs in air to remove any water crystallization. After the thermal treatment, the samples were ground into NPs powder for thermal and materials characterization. For comparison, NPs of high-entropy spinel oxide with 6 and 5 cations (HESO-6 and HESO-5), namely, $(Co_{1/6}Cr_{1/6}Cu_{1/6}Fe_{1/6}Mn_{1/6}Ni_{1/6})_3O_4$ and $(Co_{1/5}Cr_{1/5}Fe_{1/5}Mn_{1/5}Ni_{1/5})_3O_4$,[30] and a simple spinel oxide, $CuCr_2O_4$[31] were synthesized using the same method. The as-synthesized NPs of HESO-8 NPs, HESO-6, HESO-5, and $CuCr_2O_4$ were heat treated at 1000 °C in a box furnace up to 100 hrs. Their particle size changes at different time intervals were examined using scanning electron microscopy (SEM). For thermal conductivity measurements, as-prepared HESO-8 NPs were annealed in air at 1000 °C for 1 hr using a box furnace. These particles were then ground using a high-energy ball-mill (8000 M Mixer/Mill, SPEX SamplePrep) with YSZ balls in a PMMA jar. For comparison, cold-pressed pellets were also made from as-prepared NPs (i.e., after heat treatment at 550 °C for 5 hrs but without any further annealing) for thermal conductivity measurement. To make dense bulk samples using spark plasma sintering (SPS), as-synthesized NP powders were consolidated into pellets via sSPS under argon using a Thermal Technologies 3000 series SPS tool. Powders were first crushed in an agate mortar, sieved to 140 mesh, and loaded into 10 mm graphite dies lined with graphite foils. Consolidation was subsequently performed utilizing a ramp rate of 100 °C min^{-1}, and a hold time of 15 min under 50 MPa of pressure at isothermal sintering temperatures (650–1000 °C, based on sample composition). Samples were furnace-cooled under argon.

Thermal Conductivity Measurement: A Laser Flash Analyser (LFA 467HT Hyperflash, Netzsch Gerätebau GmbH) was used to measure the thermal diffusivity of all samples. A built-in "Penetration Model" in the Proteus LFA Analysis Software was used to fit the data. This model is based on ref. [45] and accounts for the penetration of the laser flash into porous samples. As-prepared powders of $CuCr_2O4$, HESO-5, 6, and 8 were uniaxially pressed into ϕ10 mm pellets using a carbon steel die and a hydraulic press. HESO-8 powder which underwent a 1 hr anneal in Air at 1000 °C and subsequently ball-milled, was measured as packed powder in a transparent Sapphire crucible (ϕ10 mm and 2 mm depth). A graphite coating was not required due to the high absorptivity and emissivity of the samples. Furthermore, this also allowed measurements under a synthetic air atmosphere.

A differential scanning calorimeter (DSC 404F1 Pegasus, Netzsch Gerätebau GmbH) was used to measure the specific heat of the dense HESO-8 sample prepared via SPS. The measurement was conducted with platinum crucibles, under a synthetic air atmosphere and a heating rate of 10 K min^{-1}. The specific heat was calculated from the ratio of a reference sapphire disc measured under the same conditions.

Thermal conductivity of the samples was then calculated as $k = \rho C_p \alpha$ (W m^{-1} K^{-1}), where ρ (kg m^{-3}) is the measured density of the sample, C_p (J kg^{-1} K^{-1}) is the specific heat obtained from DSC, and α (m^2 s^{-1}) is the thermal diffusivity obtained from LFA.

Transient Thermal Insulation Test: A home-built transient thermal insulation setup was used to examine the flame resistance and the ability of the HESO-8 NP pellets to delay thermal propagation upon sudden exposure to a high-temperature flame. In the test, the samples were fixed by stands and clamps. To avoid the direct burning a stainless-steel shim sheet of 100 mm thick was attached to the front of the side of the testing materials. The front side of as-prepared HESO-8 NP pellets (3 cm × 3 cm × 1 cm) was subjected to propane blowtorch heating (resulting in a maximum front side temperature of ≈850 °C) from a fixed distance. The backside temperature rise of HESO-8 NP pellets as a function of time was recorded using a high-temperature pyrometer (Lumasense Technologies IGA 320/23-LO). IR camera (FLIR E76 Advanced Thermal Imaging Camera) was used to capture the thermal images and temperature evolution of the HESO-8 NP pellets. For comparison, the transient thermal insulation capacity of fiberglass (10 cm × 10 cm × 1 cm), insulating refractory brick (10 cm × 10 cm × 1 cm), and ambient air were also tested. For the test of ambient air, two stainless-steel shims (10 cm × 10 cm × 100 μm) were separated by a 1 cm air gap. The backside of the stainless-steel shim sheet on the upper side was coated with a black Pyromark coating for IR thermometry of the backside temperature rise of the air gap.

Materials Characterization: The surface morphology and compositional homogeneity of HESO-8 NPs were examined by SEM (FEI Quanta 250/ Zeiss Sigma 500 SEM) equipped with energy-dispersive X-ray spectroscopy (EDS). The crystal structure of HESO-8 NPs was confirmed using the Rigaku Smartlab X-ray diffractometer (Cu Kα, $\lambda = 0.15418$ nm) as the radiation source. The diffractogram of HESO-8 was used to calculate a lattice parameter of 8.28 Å. Based on the HESO-8 spinel formula (AB_2O_4), $A = Co_{0.2}Mg_{0.2}Mn_{0.2}Ni_{0.2}Zn_{0.2}$ and $B = Al_{0.2}Co_{0.2}Cr_{0.2}Fe_{0.2}Mn_{0.2}$, the density was calculated to be roughly 5050 kg m^{-3} and assumed to be same for all synthesized HESO samples.

A Simultaneous Thermal Analyser (STA 449F5 Jupiter, Netzsch Gerätebau GmbH) was used to conduct combined TGA and differential thermal analysis (DTA) of the samples. The measurements were conducted in platinum crucibles, under synthetic air and a heating rate of 20 K min^{-1}. Commercial CuO (Ultrapure CuO, Alfa Products, #87817) was used to study the influence of copper cation.

The optical property of HESO-8 NPs was studied using a home-built UV–visible (UV)–infrared (IR) reflectance measurement system. An integration sphere (4″ LabSphere, Spectraflect coated) was assembled with an Andor Shamrock 303i spectrometer which was equipped with Si-based (Newton 920 CCD detector) and InGaAs-based (iDus InGaAs 2.2 array detector) detectors for visible–IR reflectance measurement. To characterize the optical property of HESO-8 NPs, an incident light from a supercontinuum white laser (SuperK COMPACT) was focused onto the sample surface which was contained within the integration sphere capable of collecting all angles of scattered light in the spectral range of 400–2000 nm at room temperature.

Nanoindentation tests were conducted on spinel oxide NP pellets after the high-temperature MPR measurements to determine their mechanical properties, including elastic modulus (E) and hardness (h), using an iMicro instrument (from KLA Inc.) equipped with a Berkovich tip (Type TB30524) capable of applying a maximum load of 50 mN. The Advanced E and H option was employed, maintaining a constant strain rate of 0.1 s^{-1}. The test proceeded until either the target indentation depth or indentation load was achieved. The InView software (RunTest and ReviewData modules) facilitated testing and subsequent data analysis. To minimize thermal drift, it was ensured that it remained below 0.05 nm s^{-1} throughout the testing process. Due to the inhomogeneity of the materials, multiple locations (12–15) were probed on each sample through nanoindentation tests. An oscillatory load was applied during the loading curve, with E and h determined during the unloading cycle. The load–displacement curves of

the pellets as a function of different target indentation depths are included in Figure S9 (Supporting Information).

Supporting Information

Supporting Information is available from the Wiley Online Library or from the author.

Acknowledgements

This material is based upon work supported by the U.S. Department of Energy's Office of Energy Efficiency and Renewable Energy (EERE) under Solar Energy Technologies Office (SETO) Agreement No. DE-EE0009825. The thermal characterization portion of the work was supported by the National Science Foundation (Grant No. DMR-2005181). The views expressed herein do not necessarily represent the views of the U.S. Department of Energy or the United States Government. J.L. and S.S. also acknowledge support from the Army Research Office (ARO Grant No. W911NF2210071) for research on HEGBs and stabilizing nanoalloys at high temperatures. This work was performed in part at the San Diego Nanotechnology Infrastructure (SDNI) of UCSD, a member of the National Nanotechnology Coordinated Infrastructure, which was supported by the National Science Foundation (Grant No. ECCS-2025752).

Conflict of Interest

The authors declare no conflict of interest.

Author Contributions

K.M.C., S.R.A., and Y.P. contributed equally to this work. R.C. conceived the idea and supervised the project. K.M.C., S.R.A., and Y.P. synthesized and characterized the materials and performed the thermal transport and insulation measurements. S.S. and W.H. assisted in the material synthesis and characterization. R.H.Y. and S.C. performed the mechanical tests and analysis. L.C. and Z.L. performed the optical measurements and analysis. J.L. contributed to the idea of thermal stability of HESO NPs. K.M.C. and R.C. wrote the initial manuscript. K.M.C., S.R.A and Y.P. led the writing of the revised manuscript. All the authors contributed to the editing of the manuscript.

Data Availability Statement

The data that support the findings of this study are available from the corresponding author upon reasonable request.

Keywords

high entropy oxide, high temperature, spinel oxide, thermal diffusivity, thermal insulation

Received: May 11, 2024
Revised: December 18, 2024
Published online:

[1] W. Villasmil, L. J. Fischer, J. Worlitschek, *Renewable Sustainable Energy Rev.* **2019**, *103*, 71.
[2] D. R. Clarke, M. Oechsner, N. P. Padture, *MRS Bull.* **2012**, *37*, 891.
[3] P. Singh, N. Q. Minh, *Int. J. Appl. Ceram. Technol.* **2004**, *1*, 5.
[4] P. Nambisan, H. Manjunatha, P. Ravadi, H. P. Reddy, G. Bharath, M. A. Kulkarni, S. Sundaram, *J. Energy Storage* **2023**, *74*, 109414.
[5] a) J. Niu, S. Deng, X. Gao, H. Niu, Y. Fang, Z. Zhang, *J. Energy Storage* **2022**, *47*, 103557; b) L. Li, C. Xu, R. Chang, C. Yang, C. Jia, L. Wang, J. Song, Z. Li, F. Zhang, B. Fang, *Energy Storage Mater.* **2021**, *40*, 329.
[6] Z. Yu, Y. Wan, Y. Qin, J.-P. Guan, X.-W. Cheng, X. Wang, S. Ouyang, X. Qu, Z. Zhu, J. Wang, *Chem. Eng. J.* **2023**, *477*, 147187.
[7] V. T. Le, N. San Ha, N. S. Goo, *Composites, Part B* **2021**, *226*, 109301.
[8] O. Uyanna, H. Najafi, *Acta Astronaut.* **2020**, *176*, 341.
[9] C. Ercol, E. Congdon, K. Balakrishnan, G. A. Holtzman, presented at 51st Int. Conf. Environmental Systems, July 10-14, Saint Paul, Minnesota, USA **2022**
[10] K. Schlichting, N. Padture, P. Klemens, *J. Mater. Sci.* **2001**, *36*, 3003.
[11] S. Shin, Q. Wang, J. Luo, R. Chen, *Adv. Funct. Mater.* **2020**, *30*, 1904815.
[12] D. G. Cahill, R. O. Pohl, *Phys. Rev. B* **1987**, *35*, 4067.
[13] Y. X. Luo, X. L. Yang, T. L. Feng, J. Y. Wang, X. L. Ruan, *Nat. Commun.* **2020**, *11*, 2554.
[14] X. Xu, Q. Zhang, M. Hao, Y. Hu, Z. Lin, L. Peng, T. Wang, X. Ren, C. Wang, Z. Zhao, C. Wan, H. Fei, L. Wang, J. Zhu, H. Sun, W. Chen, T. Du, B. Deng, G. J. Cheng, X. Duan, *Science* **2019**, *363*, 723.
[15] L. Su, H. Wang, M. Niu, X. Fan, M. Ma, Z. Shi, S.-W. Guo, *ACS Nano* **2018**, *12*, 3103.
[16] S. Yoon, G. D. Han, D. Y. Jang, J. W. Kim, D. H. Kim, J. H. Shim, *J. Alloys Compd.* **2019**, *806*, 1430.
[17] Y.-L. He, T. Xie, *Appl. Therm. Eng.* **2015**, *81*, 28.
[18] Y. Chen, O. Ola, G. Liu, L. Han, M. Z. Hussain, K. Thummavichai, J. Wen, L. Zhang, N. Wang, Y. Xia, *J. Eur. Ceram. Soc.* **2021**, *41*, 3970.
[19] Q. Zhang, M. Hao, X. Xu, G. Xiong, H. Li, T. S. Fisher, *ACS Appl. Mater. Interfaces* **2017**, *9*, 14232.
[20] Y. Liu, Y. Liu, W. C. Choi, S. Chae, J. Lee, B.-S. Kim, M. Park, H. Y. Kim, *J. Mater. Chem. A* **2017**, *5*, 2664.
[21] T. Shimizu, K. Matsuura, H. Furue, K. Matsuzak, *J. Eur. Ceram. Soc.* **2013**, *33*, 3429.
[22] J.-W. Wu, W.-F. Sung, H.-S. Chu, *Int. J. Heat Mass Transfer* **1999**, *42*, 2211.
[23] a) B. Wicklein, A. Kocjan, G. Salazar-Alvarez, F. Carosio, G. Camino, M. Antonietti, L. Bergström, *Nat. Nanotechnol.* **2015**, *10*, 277; b) S. Liu, J. Duvigneau, G. J. Vancso, *Eur. Polym. J.* **2015**, *65*, 33.
[24] F. Hu, S. Wu, Y. Sun, *Adv. Mater.* **2019**, *31*, 1801001.
[25] T. Xie, Y.-L. He, Z.-J. Hu, *Int. J. Heat Mass Transfer* **2013**, *58*, 540.
[26] R. Prasher, *Phys. Rev. B* **2006**, *74*, 165413.
[27] X. J. Hu, R. Prasher, K. Lofgreen, *Appl. Phys. Lett.* **2007**, *91*, 203113.
[28] P. G. de Gennes, *Rev. Mod. Phys.* **1999**, *71*, S374.
[29] M. Fracchia, M. Manzoli, U. Anselmi-Tamburini, P. Ghigna, *Scr. Mater.* **2020**, *188*, 26.
[30] J. Dabrowa, M. Stygar, A. Mikula, A. Knapik, K. Mroczka, W. Tejchman, M. Danielewski, M. Martin, *Mater. Lett.* **2018**, *216*, 32.
[31] E. B. Rubin, Y. Chen, R. Chen, *Sol. Energy Mater. Sol. Cells* **2019**, *195*, 81.
[32] M. Moner-Girona, A. Roig, E. Molins, E. Martınez, J. Esteve, *Appl. Phys. Lett.* **1999**, *75*, 653.
[33] a) G. Zu, J. Shen, L. Zou, W. Wang, Y. Lian, Z. Zhang, A. Du, *Chem. Mater.* **2013**, *25*, 4757; b) Y. Si, X. Wang, L. Dou, J. Yu, B. Ding, *Sci. Adv.* **2018**, *4*, eaas8925; c) Y. Si, J. Yu, X. Tang, J. Ge, B. Ding, *Nat. Commun.* **2014**, *5*, 5802; d) L. Wang, J. Feng, Y. Jiang, L. Li, J. Feng, *RSC Adv.* **2019**, *9*, 7833.
[34] R. Prasher, *Nano Lett.* **2005**, *5*, 2155.

[35] a) M. Tychanicz-Kwiecień, J. Wilk, P. Gil, *J. Thermophys. Heat Transfer* **2019**, *33*, 271; b) Y. Asakuma, Y. Kanazawa, T. Yamamoto, *Int. J. Heat Mass Transfer* **2014**, *73*, 97.
[36] R. Schmidt-Whitley, M. Martinez-Clemente, A. Revcolevschi, *J. Cryst. Growth* **1974**, *23*, 113.
[37] A. Rai, T. Feng, D. Howard, D. Hun, M. Zhang, H. Zhou, S. S. Shrestha, *Comput. Therm. Sci.* **2021**, *13*, 19.
[38] K. M. Chung, J. Zeng, S. R. Adapa, T. Feng, M. V. Bagepalli, P. G. Loutzenhiser, K. J. Albrecht, C. K. Ho, R. Chen, *Sol. Energy Mater. Sol. Cells* **2021**, *230*, 111271.
[39] a) Z. Zhao, H. Xiang, F.-Z. Dai, Z. Peng, Y. Zhou, *J. Mater. Sci. Technol.* **2019**, *35*, 2647; b) C. Oses, C. Toher, S. Curtarolo, *Nat. Rev. Mater.* **2020**, *5*, 295.
[40] N. Zhou, T. Hu, J. Huang, J. Luo, *Scr. Mater.* **2016**, *124*, 160.
[41] a) S. Hou, X. Ma, Y. Shu, J. Bao, Q. Zhang, M. Chen, P. Zhang, S. Dai, *Nat. Commun.* **2021**, *12*, 5917; b) A. Mehta, Y. H. Sohn, *Diffus. Found.* **2021**, *29*, 75.
[42] a) W. Kucza, J. Dąbrowa, G. Cieślak, K. Berent, T. Kulik, M. Danielewski, *J. Alloys Compd.* **2018**, *731*, 920; b) J. Dąbrowa, M. Zajusz, W. Kucza, G. Cieślak, K. Berent, T. Czeppe, T. Kulik, M. Danielewski, *J. Alloys Compd.* **2019**, *783*, 193; c) D. B. Miracle, O. N. Senkov, *Acta Mater.* **2017**, *122*, 448.
[43] J. Luo, N. Zhou, *Commun. Mater.* **2023**, *4*, 7.
[44] a) M. Qin, S. Shivakumar, J. Luo, *J. Mater. Sci.* **2023**, *58*, 8548; b) M. A. Adaan-Nyiak, I. Alam, E. Jossou, S. Hwang, K. Kisslinger, S. K. Gill, A. A. Tiamiyu, *Small* **2024**, *20*, 2309631.
[45] R. McMasters, J. Beck, R. Dinwiddie, H. Wang, *J. Heat Transfer* **1999**, *121*, 15.